



Optimizing carbon coating parameters for obtaining SiO₂/C anodes with improved electrochemical performance

Maria Valeria Blanco¹ · Viktor Renman¹ · Jiefang Zhu² · Frida Vullum-Bruer³ · Ann Mari Svensson¹

Received: 12 November 2020 / Revised: 14 January 2021 / Accepted: 1 February 2021 / Published online: 14 February 2021
© The Author(s) 2021

Abstract

In this work, we present a comprehensive and systematic study on the use of low-cost and highly abundant carbon precursors to obtain SiO₂/C anodes with superior electrochemical performance towards Li-ions. Different SiO₂/C composites are prepared by soaking silica nanoparticles in solutions containing 20 wt%, 40 wt%, or 60 wt% of glucose, sucrose, or cornstarch, followed by thermal decomposition of the carbohydrates at 850 °C or 1200 °C. Structural, microstructural, and textural differences on the composites derived from the different carbon coating treatments are related to the electrochemical performance of the anodes. Composites containing final carbon contents close to 15 wt% show a complete coverage of the SiO₂ particles with a nanometric carbon layer and exhibit the best electrochemical results. The increase in the annealing temperature from 850 to 1200 °C reduces the porosity of the carbon layer and increases its level of ordering, both having positive effects on the overall electrochemical performance of the electrodes. SiO₂/C composites coated with 40 wt% sucrose and heat treated at 1200 °C display the best electrochemical performance, delivering a reversible specific capacity of 723 mAhg⁻¹ at 50 mA g⁻¹ after 100 cycles, which is considerably higher than the reversible capacity of 233 mAhg⁻¹ obtained with the uncoated material cycled under the same conditions.

Keywords Silica anode · Carbon coating · Lithium-ion batteries · Silica activation

Introduction

Li-ion batteries (LIBs) displaying high power and energy densities are in great demand for a wide variety of energy storage applications, ranging from portable electronics and electric vehicles to grid-level energy storage. For the negative electrode, graphite is the active material of choice in conventional LIBs since it presents a low and flat potential plateau during discharge, together with high stability and low price. Graphite is able to store lithium via intercalation

in its 2D host structure, displaying a maximum theoretical capacity of 372 mAhg⁻¹. However, due to its limited capacity and the fact that it has been listed as a critical raw material by the European Commission [1, 2], new anode candidates need to be explored in order to meet the growing demand of next-generation LIBs [3].

In this context, silicon has emerged as a very promising material, exhibiting a maximum theoretical capacity of 4200 mAhg⁻¹ together with low operating potentials [4–7]. However, the alloying reaction of Si with lithium to form the fully lithiated Li₂₂Si₅ phase entails a volume expansion of about 300% which, upon repeated alloying/dealloying cycles, provokes stress accumulation, irreversible lattice deformation, and particle cracking. These structural and microstructural changes in the electroactive material cause a continuous fracture and re-formation of the SEI layer [8]. As a consequence, particles form agglomerates and lose electrical contact with the conductive additives and current collector, which results in a drastic capacity and power fade [9–12]. To overcome these shortcomings, several studies have focused on controlling Si particle size [11, 12] and on developing different coating approaches.

✉ Maria Valeria Blanco
maria.v.blanco@ntnu.no

¹ Department of Materials Science and Engineering, Norwegian University of Science and Technology, NO-7491 Trondheim, Norway

² Department of Chemistry-Ångström Laboratory, Uppsala University, Box 538, SE-75121 Uppsala, Sweden

³ Department of Thermal Energy, SINTEF Energy Research, NO-7034 Trondheim, Norway

Alternatively, SiO₂ is been tested as a potential anode candidate for next-generation LIBs [13–15]. Silica is able to react with lithium at relatively low potentials and presents a theoretical capacity of 1965 mAhg⁻¹. Besides, it is one of the most abundant materials in the Earth's crust, which is highly desirable from a large-scale application perspective. Theoretical results of DFT calculations revealed that upon electrochemical cycling, SiO₂ undergoes a variety of reversible and irreversible reactions through which Si is generated as a co-product [16]. The on-site produced Si would then reversibly react with lithium, being the main contributor to the high storage capacities displayed by SiO₂ electrodes. In parallel, the electrochemically inactive products formed upon SiO₂ lithiation would serve as a buffer to accommodate the volume changes derived from Si alloying/dealloying, therefore extending the cycling lifetime of the anodes.

In addition to Si and SiO₂, other potentially high-capacity materials include a range of oxides as conversion or insertion-type materials, such as MoO₂, Fe₂O₃, TiO₂, and SnO₂. However, one of the main drawbacks to overcome when integrating the above-mentioned materials to the battery technology is their intrinsic poor conductivity, which is detrimental for the electrochemical performance of the electrodes. Due to this, particles are often coated with an electronically conductive carbon layer. In addition to the conductive effect, carbon coating inhibits particle sintering, introduces pores and voids that provide extra space to accommodate volume variations of the active material, and prevents direct contact with the electrolyte, thereby improving the long-term cyclability and rate capability of electrodes. In the case of SiO_x and SiO₂ materials, several reports have shown the feasibility of using simple carbon coating processes for improving the electrochemical performance of the resulting electrodes [17–27]. To ensure a cost-effective, scalable, and sustainable coating approach that can be easily integrated into current battery production schemes, the use of affordable and naturally abundant carbon precursors is highly important. In addition to this, the selection of coating methods that avoid the handling of organic solvents, the release of toxic compounds, or the use of complex chemistry routes or equipment is considered an important advantage.

Among carbonaceous materials, graphene and carbon nanotubes have been widely studied as coating of negative electrodes [28]. However, owing to their low cost and wide availability, amorphous carbons easily obtained from sugars and polymers are pinpointed as very convenient options [29]. Regarding coating procedures, the thermal reduction method in which particles are impregnated or soaked into solutions containing the dissolved carbon precursor, followed by its thermal decomposition at the surface of the particles is a well-established, scalable, and cost-effective option for producing core-shell-structured carbon-coated materials [30, 31]. Indeed, the annealing of mixtures of metal oxides and carbon

sources has been successfully used for the fabrication of several carbon-coated metal oxide composites, such as Fe₃O₄/C [32, 33], Li₄Ti₅O₁₂/C [34], MoO₂/C [35], SnO₂/C [36], and ZnFe₂O₄/C [37]. Interestingly, the amount of carbon on the composites necessary to ensure a high-rate performance can be significantly reduced provided that the carbon structure is optimized [38]. In this regard, the fine-tuned structure of the carbon shell should present high electrical conductivity and favor Li-ion movement [39, 40].

In view of the great benefits of thermally driven coatings using low-cost carbon precursors for obtaining electrode materials with superior electrochemical performance, a comprehensive understanding of the extent to which variations in the coating parameters influence the properties of the coating layer, and how this relates to the electrochemical performance, is of critical importance. SiO₂ anodes are perfectly suited for this kind of study since silica does not experience huge volume variations upon cycling that can lead to rapid deterioration and fracture of the coating layer [41]. Importantly, the results derived from this kind of analysis can be also extended to metal oxide systems.

In this work, we present a comprehensive and systematic study of the carbon coating of silica anodes. Cheap carbohydrates of different carbon chain length are chosen as carbon sources, and the carbon content on the composites is controlled by changing the relative amount of the carbon precursor. SiO₂/C composites are obtained by mixing SiO₂ nanoparticles with 20 wt%, 40 wt%, or 60 wt% of glucose, sucrose, or cornstarch and heat treating the resulting SiO₂/carbon mixtures at 850 °C or 1200 °C. The annealing temperatures were chosen based on preliminary results, so that significant differences on the coating layer are obtained. The structural, microstructural, textural, and electrochemical properties of the SiO₂/C composites are characterized in order to select the most suitable carbon precursor and to determine the carbon content and structure that yields the best electrochemical performance. Since the capacity-climbing phenomenon exhibited by SiO₂ anodes [23, 27, 42–44] might complicate the identification of the composites delivering highest reversible capacity, we propose an electrochemical activation procedure that enables reaching the maximum specific capacity after 3 cycles.

Results and discussion

Characterization of uncoated SiO₂ particles

A SEM image of as-received silica particles is shown in Fig. 1a. The particles present a spherical shape and a size distribution ranging from 100 to 800 nm, with an average size of 340 nm, as it can be observed from the inset graph. The X-ray diffraction pattern displayed in Fig. 1b shows a broad peak at $Q=1.7 \text{ \AA}^{-1}$, which is indicative of amorphous silica,

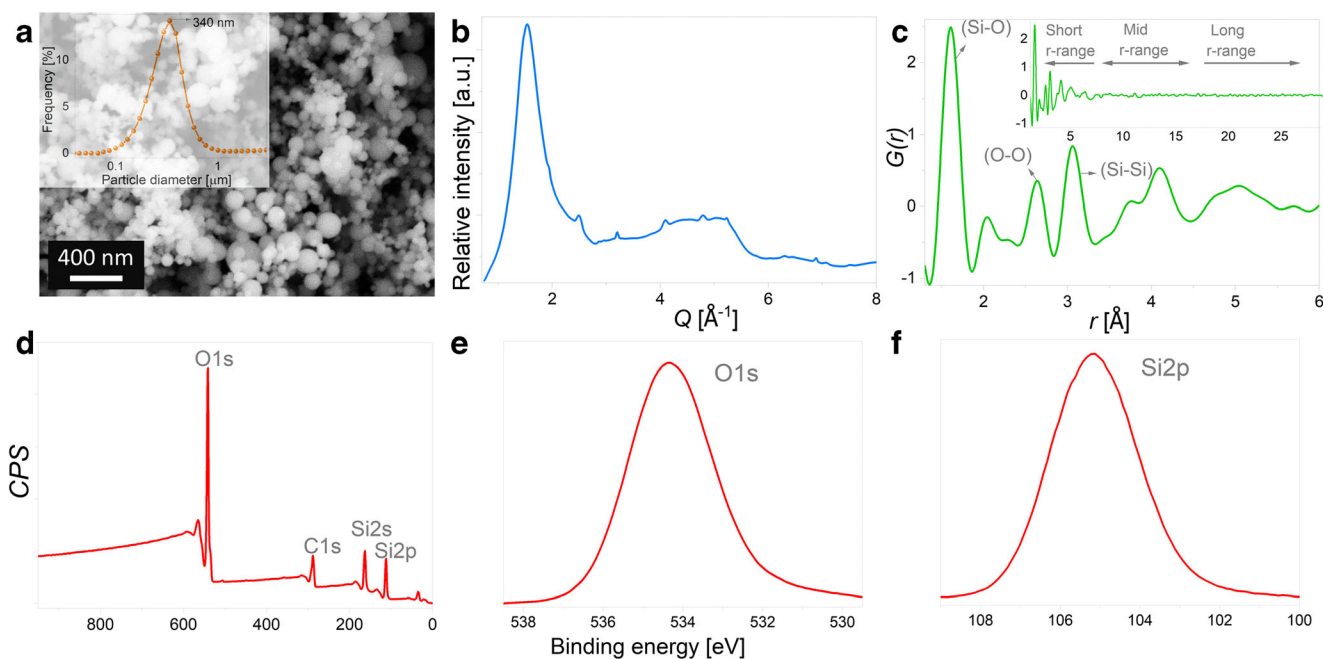


Fig. 1 Characterization of SiO₂ particles. (a) SEM micrograph and inset graph showing the particle size distribution curve, (b) X-ray diffraction pattern, (c) pair distribution function plot, (d) XPS survey spectrum, (e) XPS high-resolution spectrum of O1s, and (f) XPS high resolution spectrum of Si2p

together with various smaller reflections corresponding to SiC impurity. The pair distribution function plot obtained from total scattering measurements, depicted in Fig. 1c shows the presence of peaks at bond distances typical of SiO₂ local structure [45]. The first peak at $r=1.60$ Å is associated to first-order Si–O pairs, while peaks at $r=2.62$ Å and $r=3.07$ Å correspond to first order O–O and Si–Si pairs, respectively. The complete pair distribution function plot is presented in the inset graph of the same figure and evidences the lack of mid- and long-range ordering of the material. Elemental composition analysis performed by ICP-MS (oxygen not included) revealed that 97.1% of the material is composed of Si, while Fe, K, Ca, and Na are present in low amounts (less than 1%). The composition and chemical oxidation state at the surface of silica particles were determined by XPS, in the range from 0 to 1200 eV. The survey spectrum displayed in Fig. 1d shows the presence of four main peaks at binding energies of 532.5 eV, 285.1 eV, 154.2 eV, and 103.1 eV, which correspond to O1s, C1s, Si2s, and Si2p, respectively. Quantitative atomic composition analysis yielded the following atomic percentages: 68.60% O, 15.95% Si, 15% C, and 0.45% Na. The significant amount of carbon found at the surface of the particles is attributed to adventitious carbon contamination. The high-resolution regional scans corresponding to O1s and Si2p are depicted in Fig. 1e and f, respectively, and show good correspondence with previous results obtained on SiO₂ samples [27].

An initial assessment of the electrochemical properties of uncoated SiO₂ particles was performed in order to later

determine the effect of carbon coating. Prior to electrochemical testing, the electrodes were subjected to an electrochemical activation procedure. The activation consisted in performing 3 lithiation-delithiation cycles between 0.002 (vs. Li⁺/Li) and 2 V (vs. Li⁺/Li) at a constant current of 10 mA g⁻¹. After completion of each half cycle, the low and high cut-off voltages were held for 48 h. This procedure is a modification of the time-limited potentiostatic discharge method proposed by Lepoivre and co-workers [46] and allows to significantly diminish the capacity-climbing behavior upon prolonged cycling, related to the conversion of SiO₂ to Si, Li₂O, Li₂Si₂O₅, and Li₄SiO₄.

A specific capacity of 459 mAhg⁻¹ is achieved after the first lithiation (Fig. 2a) and the differential capacity plot corresponding to this stage (Fig. 2b) shows the occurrence of two small broad reduction peaks at 1.45 V and 1.25 V, and a more pronounced and sharper peak at 0.83 V. The peaks at higher potentials are associated to irreversible conversion reactions between the electrode and the electrolyte, while the peak at 0.83 V can be attributed to electrolyte decomposition reactions and formation of the SEI [14, 42]. The following delithiation step displays a capacity of 209 mAhg⁻¹, which increases to 331 mAhg⁻¹ in the 3rd cycle. This is accompanied with an increase in the coulombic efficiency from 45 to 95% and a growth of anodic and cathodic peaks at 0.3 V and 0.44 V, and 0.03 V and 0.15 V, respectively, all of them characteristic of silicon lithiation/delithiation reactions [47, 48]. Once the activation step was concluded, the electrode was subjected to galvanostatic cycling at 50 mA g⁻¹. The voltage profile

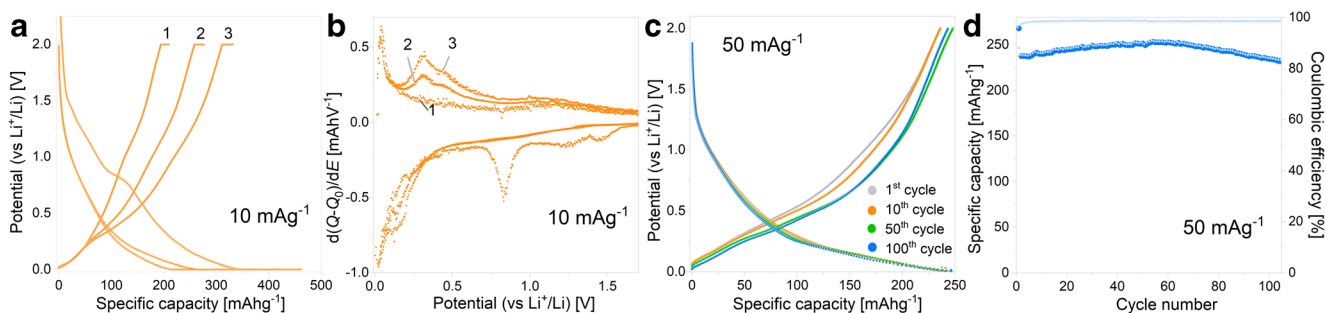


Fig. 2 (a, b) Voltage profile curves and differential capacity plots, respectively, of SiO₂ electrodes during activation step at 10 mA g⁻¹. (c, d) Voltage profile curves and specific capacity vs cycle number plots, respectively, corresponding to galvanostatic cycling at 50 mA g⁻¹

curves (Fig. 2c) evidence a continuous variation towards the conformation of more defined quasi-plateaus at potentials below 1 V over the first 50 cycles. Accordingly, the specific capacity increases from 238 to 252 mAhg⁻¹ (Fig. 2d). This 5% increment indicates that the activation step strongly reduced the capacity-climbing phenomena, since further cycling did not lead to significant capacity gains.

In the following sections, the effect of carbon coating on SiO₂ particles with different amounts and types of carbon precursors and annealing temperatures will be evaluated. For clarity, the SiO₂/C composites obtained as a result of the different carbon coating treatments will be referred to as presented in Table 1.

Effect of carbon coating precursor

Gas adsorption analysis results of SiO₂/C composites annealed at 850 °C (Fig. 3a) show an increasing trend of external surface and micropore area with increasing amounts of carbon precursor. The pores are formed as a consequence of the carbohydrate decomposition at the surface of the particles during the annealing step, which causes the release of gases.

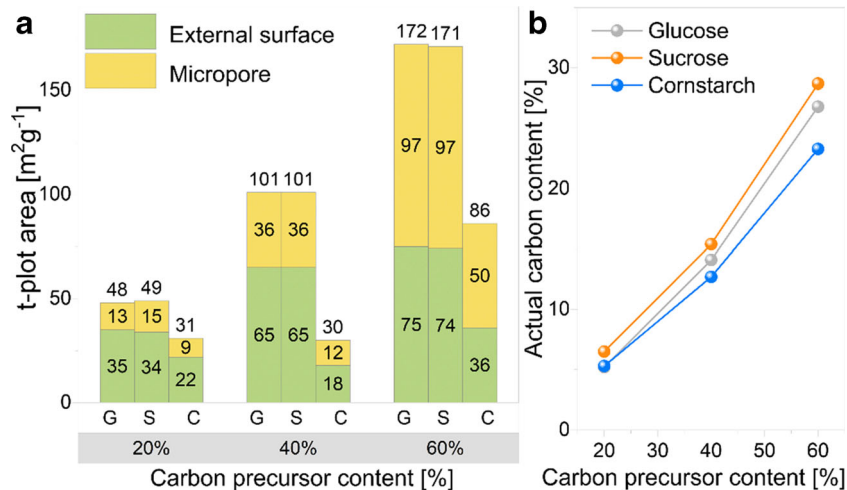
Table 1 Nomenclature of SiO₂/C composites subjected to different carbon coating treatments. *G* glucose, *S* sucrose, *C* cornstarch, *C.P.* carbon precursor, *A.T.* annealing temperature

Nomenclature	C.P.	C.P. amount (wt%)	A.T. (°C)
G40@850	glucose	40	850
S20@850	sucrose	20	850
S40@850	sucrose	40	850
S60@850	sucrose	60	850
C40@850	cornstarch	40	850
G40@1200	glucose	40	1200
S20@1200	sucrose	20	1200
S40@1200	sucrose	40	1200
S60@1200	sucrose	60	1200
C40@1200	cornstarch	40	1200

For composites coated with 60 wt% of carbon precursor, the micropore area is in all cases significantly higher than the external surface area. This reveals the highly porous nature of the coating layer covering the particles. Interestingly, composites coated with glucose and sucrose exhibit similar micropore and external area values, whereas composites coated with cornstarch display much lower values. N₂ adsorption-desorption isotherms depicted in Figure S1 of the Electronic Supplementary Material (ESI) indicate that the type II isotherms displayed by the uncoated SiO₂ particles, which are characteristic of monolayer-multilayer adsorption on non-porous materials, evolve to type IV curves with H2 hysteresis loops after carbon coating. The latter is indicative of capillary condensation in the mesopores. Also, the pore size distribution curves of coated composites, shown in the same figure, display a marked growth of pores with a diameter size below 5 nm with increasing amounts of carbon precursor.

The actual carbon content of the composites shows an exponential dependence with the carbon precursor amount (Fig. 3b). Carbon retention is higher for SiO₂/sucrose composites and significantly lower for SiO₂/cornstarch composites. S20@850, S40@850, and S60@850 display actual carbon contents of 6.5 wt%, 15.4 wt%, and 28.7 wt%, respectively, while C20@850, C40@850, and C60@850 show a carbon retention of 5.3 wt%, 12.7 wt%, and 23.3 wt%, respectively. Interestingly, the observed results show good agreement with the solubility degree of the carbon precursors in water. Glucose and sucrose are polar molecules that easily dissolve in water. However, the amount of polar hydroxyl groups that can hydrogen-bond with water is higher for sucrose [8] than for glucose [5], and therefore the solubility of sucrose in water is significantly higher than the solubility of glucose (about 2000 gL⁻¹ against 909 gL⁻¹, respectively, at 25 °C). On the other hand, cornstarch does not dissolve in water but forms a dispersion. In view of this, it can be argued that when particles are soaked in solutions containing highly soluble carbohydrates, a higher amount of carbon precursor will uniformly cover their surfaces, therefore enhancing the carbon retention after the annealing treatment. The potential agglomeration of non-dissolved cornstarch particles at the SiO₂ surface might

Fig. 3 (a) External surface and micropore area and (b) actual carbon content of SiO₂/C composites annealed at 850 °C

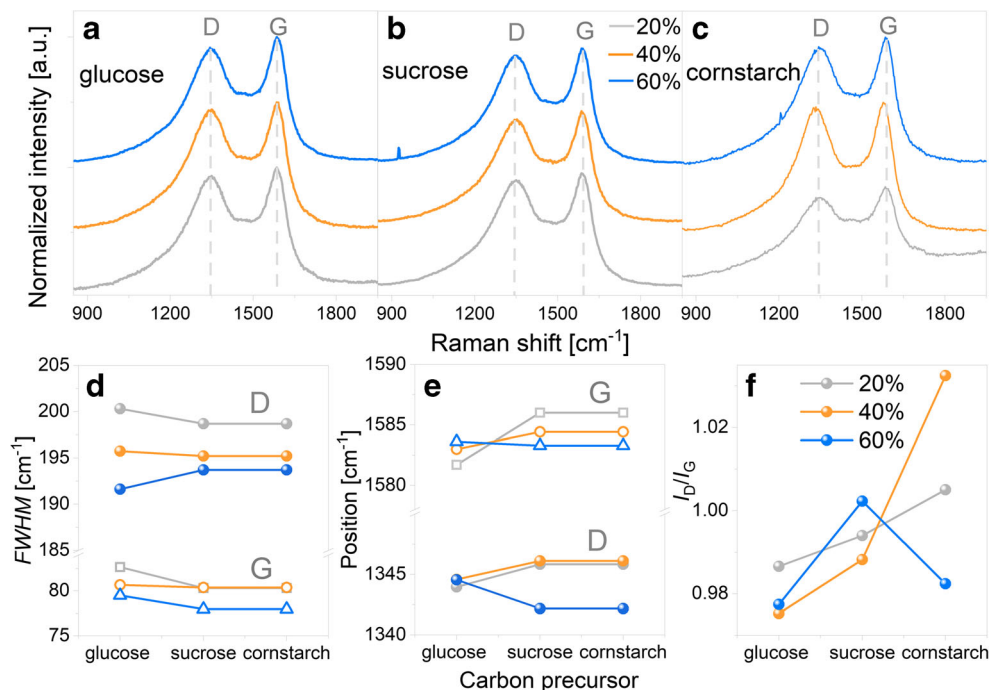


lead to a non-uniform carbohydrate distribution, which might explain the lower carbon retention and the differences in the measured area of SiO₂/cornstarch composites.

To gain insights in the nature of the carbon layer covering the particles, Raman spectroscopy measurements were performed. Raman spectra of composites coated with different amounts of glucose, sucrose, and cornstarch annealed at 850 °C are depicted in Fig. 4a, b and c, respectively. All composites exhibit the D band (1350 cm⁻¹), associated to the breathing mode of the sp² aromatic ring within a graphitic cluster, and the G band (1580 cm⁻¹), related to the in-plane sp² bond stretching shear vibration within the aromatic ring in a large, graphene-like cluster [49, 50]. In Fig. 4d, the FWHM of the D and G bands are plotted as a function of the carbon precursor. It can be observed that the variation of the FWHM among

carbon precursors is negligible. The position of the bands is very similar for sucrose and cornstarch, while there is a shift towards low frequency values for glucose (Fig. 4e). The absence of major shifts in the Raman bands suggests that there are no significant differences in the degree of order/disorder among composites containing different carbon sources. Finally, I_D/I_G ratio plots, indicative of carbon crystallization degree (Fig. 4f) exhibit values close to 1, and variations are minor for composites coated with glucose and sucrose, and higher for composites coated with cornstarch. Additional characterization by X-ray diffraction showed the retention of the amorphous silica matrix after the heat treatment (Figure S2) and element distribution maps obtained by SEM/EDX evidenced a homogeneous carbon distribution on the composites (Figure S3).

Fig. 4 Raman spectrum of SiO₂/C composites coated with different percentages of glucose (a), sucrose (b), and cornstarch (c) at 850 °C. Full width at half maximum corresponding to deconvoluted D and G bands (d), center position of D and G bands (e), and I_D/I_G ratio (f) as a function of carbon precursor



The electrochemical characterization results of the composites are summarized in Fig. 5. To compare the electrochemical performance of composites coated with different amounts of carbon precursor, Fig. 5a displays the lithiation-specific capacity and Coulombic efficiency as a function of cycle number of electrodes made of S20@850, S40@850, and S60@850. The specific capacities after 100 cycles are as follows: 600 mAhg⁻¹, 678 mAhg⁻¹, and 644 mAhg⁻¹, respectively. In all cases, the Coulombic efficiencies are above 98.5%. Rate capability results (Fig. 5b) show the following lithiation capacity values for S20@850, S40@850, and S60@850: 400 mAhg⁻¹, 483 mAhg⁻¹, and 446 mAhg⁻¹, respectively (at 0.5 Ag⁻¹), and 260 mAhg⁻¹, 319 mAhg⁻¹, and 300 mAhg⁻¹, respectively (at 2 Ag⁻¹). As can be noticed, composites coated with 20 wt% sucrose display the poorest electrochemical performance. This was also observed for composites coated with glucose and cornstarch, where the best results are achieved by coating treatments in which 40 wt% of carbon precursor is utilized.

Since composites coated with 40 wt% carbon precursor (14% actual carbon content, average value) display the best electrochemical performance, Fig. 5c and Fig. 5d present electrochemical cycling results of electrodes made of G40@850, S40@850, and C40@850. After 100 cycles, the electrodes delivered the following capacities: 640 mAhg⁻¹ (G40@850), 678 mAhg⁻¹ (S40@850), and 581 mAhg⁻¹ (C40@850). The Coulombic efficiency values are in all cases above 98.2%. Rate capability results show capacities of 442 mAhg⁻¹

(G40@850), 483 mAhg⁻¹ (S40@850), and 419 mAhg⁻¹ (C40@850) at 0.5 Ag⁻¹. Therefore, the performance of S40@850 is clearly superior in comparison with G40@850 and C40@850 electrodes.

A more detailed analysis of the results obtained with the best performing composite, S40@850, is presented in the lower part of Fig. 5. Figure 5e and f display the voltage profile curves and differential capacity plots, respectively, corresponding to the activation step of S40@850. The first lithiation exhibited a capacity of 1310 mAhg⁻¹, which is significantly higher than the 459 mAhg⁻¹ obtained with the uncoated material. The corresponding differential capacity plot shows the appearance of two anodic peaks at 1.52 V and 0.93 V, again associated to irreversible reactions and SEI formation. The following delithiation half cycle showed a capacity of 593 mAhg⁻¹, and in the 3rd activation cycle, the delithiation capacity reaches 840 mAhg⁻¹, with a Coulombic efficiency of 97.7%. Again, the development of Si alloying/dealloying characteristic peaks is observed. Upon galvanostatic cycling at 50 mA g⁻¹, a slight gradual increment in the capacity is noticed. After 100 cycles, the lithiation capacity raised from 636 to 678 mAhg⁻¹ (Fig. 5g). Again, the increase in capacity is accompanied with the growth of Si anodic and cathodic peaks (Fig. 5h). The delivered capacity is significantly higher than that of the uncoated material (234 mAhg⁻¹ after 100 cycles).

In order to demonstrate the importance of the activation procedure in diminishing the climbing capacity behavior of

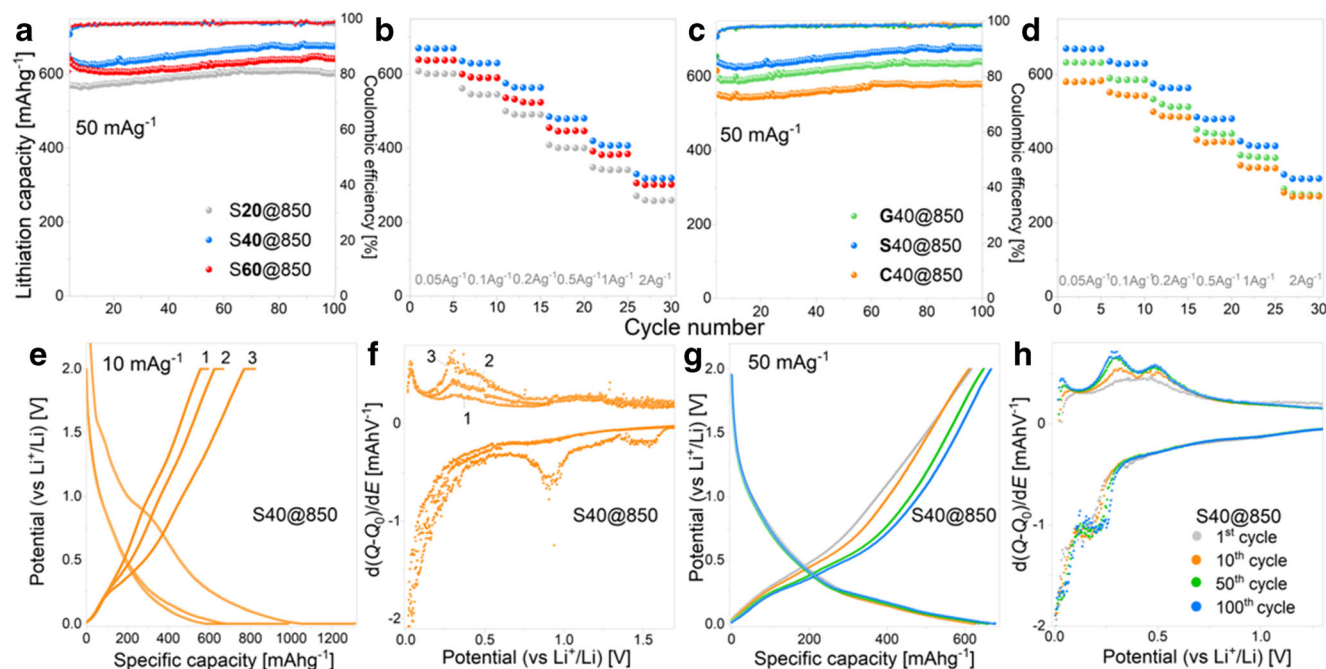


Fig. 5 (a) Lithiation capacity as a function of cycle number of S20@850, S40@850, and S60@850 cycled at 50 mA g⁻¹ (b) at variable current rates. (c) Lithiation capacity of G40@850, S40@850, and C40@850 cycled at 50 mA g⁻¹ (d) at variable current rates. (e, f) Voltage profile

curves and differential capacity plots, respectively, of S40@850 upon electrochemical activation. (g, h) Voltage profile curves and differential capacity plots, respectively, of S40@850 cycled at 50 mA g⁻¹

silica anodes, an electrode made of S40@850 composite was subjected to a first lithiation-delithiation step at 10 mA g^{-1} , followed by galvanostatic cycling at 50 mA g^{-1} . The results, depicted in Figure S4 show a Coulombic efficiency for the first cycle of 33.8%, and lithiation capacities increasing from 284 to 390 mAh g^{-1} after 100 cycles, with an averaged Coulombic efficiency of 93.2%. This not only evidences slow silica activation upon cycling but also shows the difficulty in determining the maximum deliverable capacity of the composites and the benefits of the proposed electrochemical activation procedure.

The results presented in this section indicate that composites coated with 40 wt% carbon precursor display the best electrochemical performance. Since 20 wt% of carbon precursor leads to around 5.7 wt% (average value) effective carbon content, it is possible to argue that this carbon amount might be insufficient to ensure a complete coverage of the particles. When coating with 40 wt% carbon precursor, the external surface area significantly increases while the amount of mesopores is still low. On the other hand, particles coated with 60 wt% carbon precursor suffer from large micropore area, which might be detrimental for Li-ion transport. Also, higher carbon contents would lead to thicker carbon layers, which might hinder ion transport processes. Among carbon precursors, sucrose appears as the best candidate. The superior electrochemical performance of $\text{SiO}_2/\text{sucrose}$ composites can be explained by a more effective coating and a more uniform carbon distribution on the particle surface.

Effect of carbon coating annealing temperature

In order to determine the effect of the annealing temperature on resulting carbon coating and electrochemical performance of the electrodes, a comparative analysis between composites annealed at 850°C and 1200°C is presented.

Figure 6a shows the external surface and micropore areas of composites annealed at 1200°C . In this case, regardless of

the carbon precursor amount, the exhibited micropore areas are significantly lower compared to the composites annealed at 850°C , with reductions ranging from 70 to 95%. Again, for a given carbon precursor amount, composites coated with glucose and sucrose display similar micropore and external surface area values, whereas composites coated with cornstarch exhibit significantly lower values. The external surface area of composites coated with 20 wt% and 40 wt% carbon precursor are slightly lower than their counterparts annealed at 850°C . Interestingly, for carbon precursor amounts of 60 wt%, the external surface area is dramatically reduced. The corresponding N_2 adsorption-desorption isotherms and pore size distribution curves are depicted in Figure S5.

In Fig. 6b, TGA results of composites coated with different amounts of sucrose and annealed at 850°C , 1050°C , and 1200°C are presented. The effective carbon content shows, again, an exponential dependence with the amount of carbon precursor. A 4% decrease in the carbon content of the composites is evidenced when increasing the annealing temperature from 850 to 1200°C .

To gain better insights on the changes of the coating derived from the temperature increase, examination by TEM was performed. TEM bright field micrographs of S40@850 and S40@1200 composites are presented in Fig. 7a and b, respectively. The results further demonstrate the drastic change in the porosity of the coatings and also show important variations on the carbon thickness. This can be explained by the collapse of mesopores at high annealing temperatures, followed by a compaction of the carbon. The final thickness of the carbon coating formed on S40@1200 after annealing is lower than 10 nm.

The Raman spectra corresponding to $\text{SiO}_2/\text{sucrose}$ composites annealed at 850°C , 1050°C , and 1200°C , displayed in Fig. 8a, b and c, respectively, show a noticeable narrowing of the D and G bands with increasing temperatures. This effect is quantified in Fig. 8d and is indicative of crystallite growth and a higher carbon organization. Additionally, the D band

Fig. 6 (a) External surface and micropore area of SiO_2/C composites annealed at 1200°C , (b) actual carbon content of composites coated with 20 wt%, 40 wt%, and 60 wt% of sucrose and annealed at 850°C , 1050°C , and 1200°C

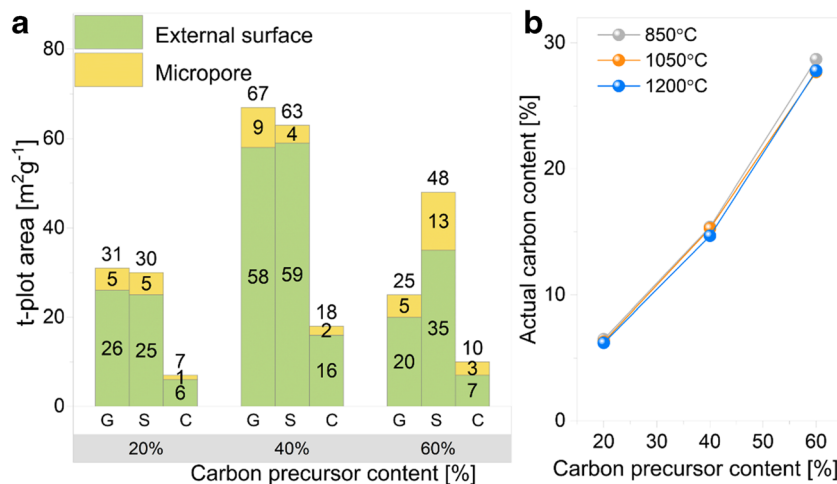
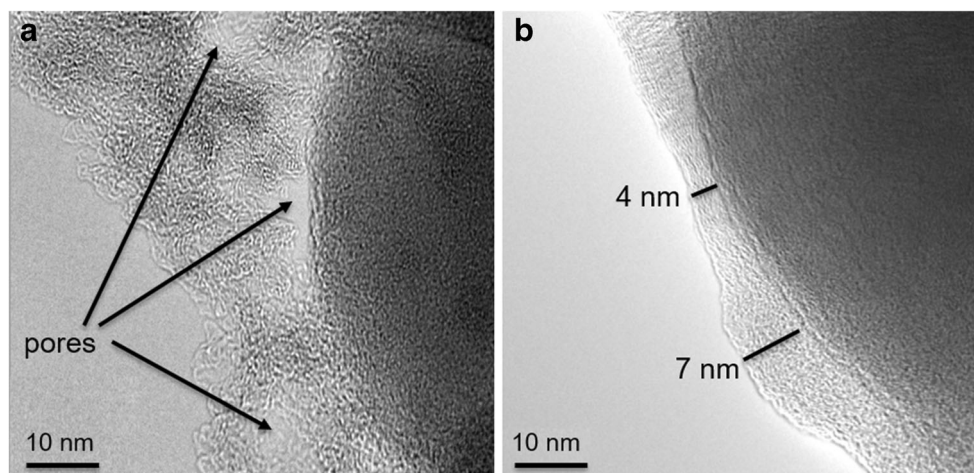


Fig. 7 TEM bright field micrographs corresponding to S40@850 (a) and S40@1200 (b)

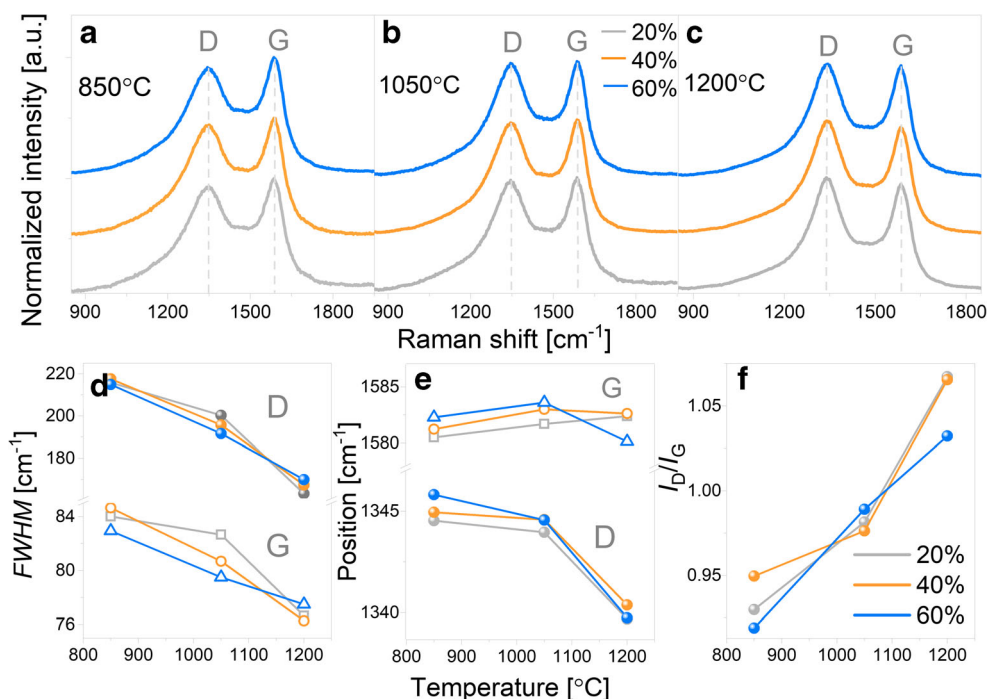


shifts to lower frequency values (Fig. 8e) with increasing annealing temperature. This change can be related to the decrease in bond-angle disorder and increase in the degree of carbon organization [51, 52]. Finally, the I_D/I_G ratio displayed in Fig. 8f exhibits a marked increase with temperature for all the composites that is associated to a growth in the number or size of the crystallites [51], which is consistent with previous reports [27, 53, 54].

Electrochemical testing results of composites annealed at 1200 °C are shown in Fig. 9. Comparisons between S20@1200, S40@1200, and S60@1200 show a trend similar to the one observed for S20@850, S40@850, and S60@850, where composites coated with 20 wt% of sucrose deliver significantly lower capacities (545 mAhg⁻¹ after 100 cycles), and

composites coated with 40 wt% of sucrose exhibit the highest capacities (723 mAhg⁻¹ after 100 cycles) (Fig. 9a). This is also valid for SiO₂/C coated with glucose and cornstarch. Figure 9b shows the cycling performance of S20@1200, S40@1200, and S60@1200 composites at different current rates. While S20@1200 exhibits significantly lower capacity values at the different rates, the superiority in terms of cycling capacity of S40@1200 over S60@1200 is almost inverted for current values above 2 Ag⁻¹. The narrowing of the capacity gap between S40@1200 and S60@1200 with increasing current rates might indicate that at sufficiently low current rates, the thin, compact, and well-structured carbon layer of the composites will provide good electronic conductivity and facilitate Li transport to the SiO₂ matrix, so that the reaction

Fig. 8 Raman spectrum of S20, S40, and S60 composites annealed at (a) 850 °C, (b) 1050 °C, and (c) 1200 °C. (d) Full width at half maximum, (e) position, and (f) I_D/I_G ratio of D and G bands against temperature



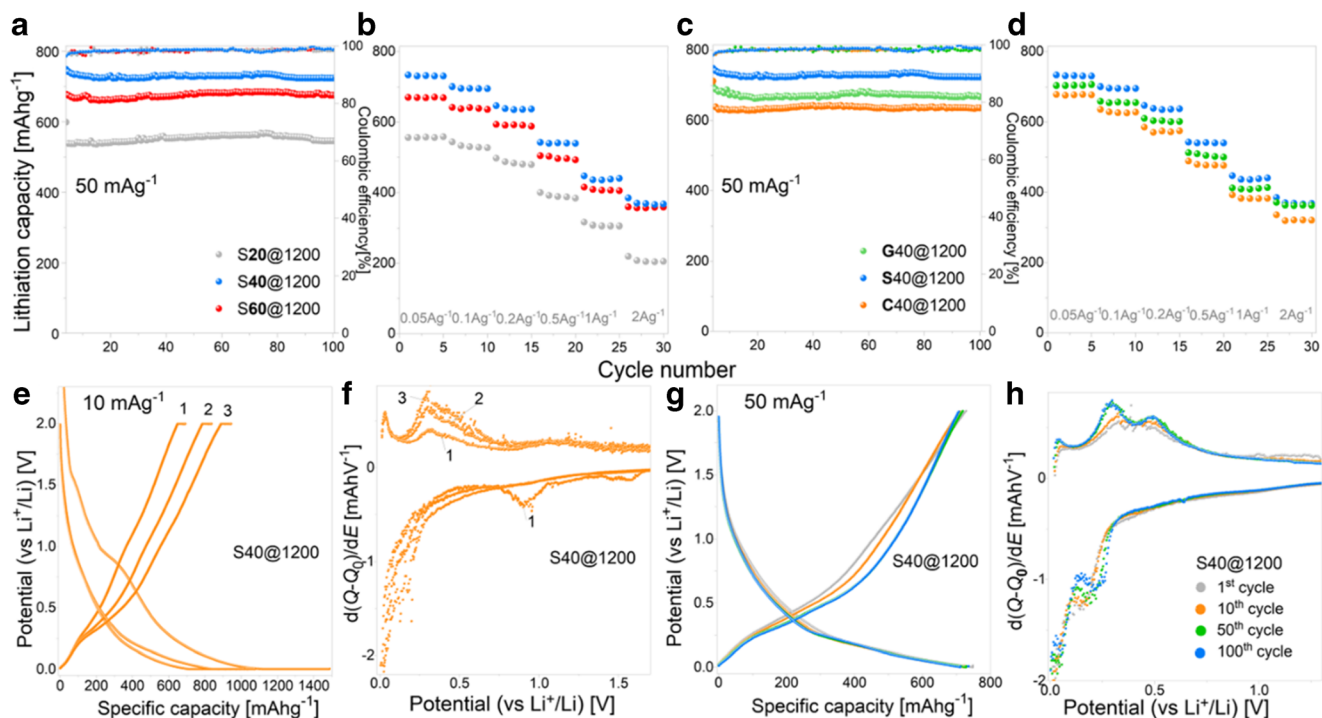


Fig. 9 (a) Lithiation capacity as a function of cycle number for S20@1200, S40@1200, and S60@1200 cycled at 50 mA g^{-1} ; (b) at variable current rates; (c) lithiation capacity of G40@1200, S40@1200, and C40@1200 cycled at 50 mA g^{-1} ; (d) at variable current rates. (e)

Voltage profile and (f) differential capacity plots of S40@1200 upon electrochemical activation, (g) voltage profiles, and (h) differential capacity plots of S40@1200 cycled at 50 mA g^{-1}

between SiO_2 and Li-ions will greatly contribute to the overall capacity of the electrodes. Contrarily, at higher current rates, carbon lithiation/delithiation might play a more preponderant role in terms of capacity contribution and Li-ions might react with a thin fraction of the SiO_2 shell. A similar behavior is also observed for composites heat-treated at 850°C .

Since composites coated with 40 wt% carbon precursor displayed the best electrochemical performance, the cycling capacities of G40@1200, S40@1200, and C40@1200 at 50 mA g^{-1} (Fig. 9c) and at varied current rates (Fig. 9d) are presented. Despite the differences observed when cycling at low current rates, the results show that at high currents, materials with glucose- and sucrose-based coatings (G40@1200 and S40@1200) display a more similar performance in comparison with composites heat treated at 850°C , indicating that a higher annealing temperature is required for the glucose precursor to develop a well-structured coating.

A more closer look at S40@1200 results shows that a lithiation capacity of 1076 mA h g^{-1} is reached in the 3rd activation cycle (Fig. 9e) together with a prominent Si alloying/dealloying footprint (Fig. 9f). Results from galvanostatic cycling at 50 mA g^{-1} (Fig. 9g and h) show less pronounced variations of the voltage profiles in comparison with S40@850. After 50 cycles, no further variations are evidenced.

With the aim of quantifying the influence of variations in carbon precursor type and amount and annealing temperature

on the electrochemical performance of the anodes, a summary of the electrochemical results obtained from this work is presented in Table 2. Clearly, the lowest capacity is delivered by uncoated SiO_2 (lithiation capacity of 234 mA h g^{-1} after 100 cycles). Among SiO_2/C composites, S20@850 and S20@1200 display the poorest electrochemical performance, 600 mA h g^{-1} and 545 mA h g^{-1} , respectively, after 100 cycles. These results suggest that 5 wt% of actual carbon content on the composites might not be enough to ensure a complete coverage of the electroactive material. Interestingly, XRD data corresponding to S20@1200 (Figure S6) show a marked crystallization of the SiO_2 matrix. In view of this, it can be stated that coatings performed with low carbon precursor amounts might not only cause particle sintering but might also favor the growth of crystalline domains at high annealing temperatures. Importantly, the delivered capacities are still 133% (S20@850) and 156% (S20@1200) higher than the capacity exhibited by uncoated SiO_2 .

When comparing composites annealed at different temperatures, materials coated with 40 wt% and 60 wt% carbon precursor and heat treated at 1200°C display improved electrochemical performances. This suggests that the carbon layer structure obtained at 1200°C leads to improved electronic conductivity throughout the composite electrode, in spite of the thinner layer. Furthermore, the higher degree of ordering of the carbon coating does not seem to reduce the ionic transport across the layer.

Table 2 Summary of the capacities (mAhg^{-1}) and Coulombic efficiencies, CE (%), of anodes made of uncoated SiO_2 and SiO_2/C composites. The values for the first cycle correspond to a cycling current of 10 mAg^{-1} . The rest of the cycling results correspond to a current of 50 mAg^{-1}

Composite	1st lithiation.	1st delithiation	CE	10th cycle	50th cycle	100th cycle	Cycling at 2Ag^{-1}
SiO_2	459	209	45.5	241	250	234	-
G40@850	1241	582	46.9	594	628	640	275
S20@850	1098	495	45.1	570	598	600	260
S40@850	1310	593	45.3	629	660	678	319
S60@850	1361	648	47.6	611	623	644	300
C40@850	1256	588	46.8	545	564	581	272
G40@1200	1190	598	50.3	673	675	668	362
S20@1200	1063	507	47.7	539	556	545	206
S40@1200	1487	690	46.4	731	727	723	369
S60@1200	1457	646	44.3	672	677	675	357
C40@1200	1260	659	52.3	644	640	632	318
S40@850*	1025	345	33.8	292	341	390	0

The Coulombic efficiency values for the first cycle range from 44.3 to 52.3% and are in line with previous reports (47% [42]). These low Coulombic efficiencies, which are still below 90% at the 3rd activation cycle, evidence the need of a pre-lithiation step in order to make use of this anode candidate. When comparing electrodes subjected to the activation procedure (S40@850) with unactivated electrodes (S40@850*), it is very clear that the CE of the first cycle is improved when incorporating potentiostatic holding steps after the first lithiation and delithiation. The unactivated material delivers a capacity of 390 mAhg^{-1} after 100 cycles, which is significantly lower than the 678 mAhg^{-1} displayed by the activated electrode. Also, S40@850* shows a marked capacity climbing behavior, with capacity increments of 37% during 100 cycles and still climbing up after 100 cycles. In the case of the activated electrodes, the capacity climbing phenomena of composites annealed at $850 \text{ }^\circ\text{C}$ shows, in average, an increase of 5% after 100 cycles and composites heat treated at $1200 \text{ }^\circ\text{C}$ display an averaged capacity increment of 0.25%. These values are significantly lower compared with previous studies where the climbing-up capacity phenomena is more pronounced (316% capacity increment after 200 cycles [45], 157% capacity increment after 70 cycles [29]) and indicate that the maximum deliverable capacity can be reached after a few cycles, provided that pre-conditioning steps in which SiO_2 particles are chemically or electrochemically activated are incorporated.

Conclusions

In this study, we prepared SiO_2/C composites by carbon coating treatments involving the thermal reduction of cheap and abundant carbohydrates, and analyzed the effect of varying the type and amount of carbon precursor and annealing temperature on the structural, microstructural, textural, and electrochemical properties of the resulting SiO_2/C anodes for

LIBs. For this, silica nanoparticles were carbon coated with 20 wt%, 40 wt%, or 60 wt% glucose, sucrose, or cornstarch and annealed at $850 \text{ }^\circ\text{C}$ or $1200 \text{ }^\circ\text{C}$.

Thermogravimetric results showed an exponential dependence of the effective carbon content in the composites with the carbon precursor amount, and a similar carbon retention for composites coated with equal amounts of different carbon precursors annealed at different temperatures. Carbon retention was found to be higher for composites coated with sucrose and lower for composites coated with cornstarch, and these differences were attributed to differences in the water solubility of the carbohydrates. A significant increase of micropore and external surface area was evidenced for increasing amounts of carbon content and a significant reduction of the porosity was achieved by increasing the annealing temperature from 850 to $1200 \text{ }^\circ\text{C}$. Raman results showed a marked increase of carbon organization degree with increasing temperatures.

Composites containing $\sim 15 \text{ wt\%}$ of carbon content displayed the best electrochemical performance. Among carbon precursors, particles coated with sucrose showed highest specific capacity and best rate performance. Reducing the porosity and enhancing carbon ordering by increasing the annealing temperature helped to increase ion and electronic conductivity, and therefore to improve the electrochemical performance of the electrodes.

Experimental

Preparation of SiO_2/C composites

Silica particles (Elkem) were carbon-coated with 20 wt%, 40 wt%, or 60 wt% of glucose (Sigma-Aldrich), sucrose (Sigma-Aldrich), or cornstarch (Carl Roth GmbH, 99.3%) using the

following procedure: [1] dissolution of the carbon precursor in distilled water, [2] addition of SiO₂ particles, [3] 30-min ultrasonication, [4] 2 h of continuous stirring in a hot plate at 60 °C, and [5] manual grinding with an agate mortar. The resulting powders were loaded into alumina crucibles and annealed at 850 °C or 1200 °C under 80 Lh⁻¹ Ar flow during 6 h.

Materials characterization

The elemental composition of SiO₂ particles was determined by inductively coupled plasma mass spectrometry (ICP-MS). Further elemental analysis was performed by XPS measurements (Kratos Analytical Axis Ultra DLD) using an Al monochromatic X-ray source operating at 100 W. Particle size was measured by laser diffraction (Horiba Partica LA-960 Laser Scattering Particle Size Distribution Analyzer). The structure of the material was analyzed by X-ray synchrotron total scattering measurements at the beamline P02.1 of DESY, at a beam energy of 60 KeV. Carbon content in the composites was determined by thermal gravimetric analysis, using a TGA/DTA probe (NETZSCH STA 449 Jupiter). The material morphology was examined by SEM (FE-SEM Zeiss Ultra 55). ESPRIT software (Bruker) was employed to obtain energy-dispersive X-ray image maps. Transmission electron microscopy micrographs were collected using a JEM-2100 Transmission Electron Microscope with LaB₆ filament. N₂ adsorption-desorption isotherms were measured at 77 K using a Tristar 3000 Surface Area and Porosity Analyzer. Prior to the measurements, samples were out-gassed under vacuum at 250 °C for 12 h. Raman spectra were recorded at room temperature (Alpha300M confocal Raman microscope, WiTec), using an excitation wavelength of 532.1 nm. Quantitative analysis of first-order Raman spectroscopy results was performed by deconvolution of the acquired spectra via multiple curve fitting with Lorentzian function, using Fityk software [55]. XRD measurements of the composites were performed using a Bruker D8 A25 DaVinci X-ray Diffractometer with CuK α radiation.

Electrode preparation and electrochemical characterization

Slurries containing 50 wt% of SiO₂ (Elkem) or SiO₂/C composites, 35 wt% carbon black (Timcal C-ENERGYTM C65), and 15 wt% of sodium alginate binder (Sigma-Aldrich) were ball-milled at 25 Hz for 45 min (Retsch Shaker 400 MM) and tape-casted onto 18- μ m-thick Cu foils (Schlenk Metallfolien). Electrodes were dried under vacuum overnight at 120 °C and then transferred to an Ar-filled glove box for further assembling into coin cells, using lithium foil (0.75 μ m thick) as counter electrode and 1 M LiPF₆ in 50:50 vol.% EC:DEC

electrolyte (Sigma-Aldrich). The electrochemical performance of the electrodes was evaluated by performing galvanostatic charge-discharge tests between 0.002 and 2 V versus Li⁺/Li, at 10 mA g⁻¹ and 50 mA g⁻¹. Rate capability tests were performed at varied currents of 50 mA g⁻¹, 100 mA g⁻¹, 200 mA g⁻¹, 500 mA g⁻¹, 1000 mA g⁻¹, and 2000 mA g⁻¹ using a Biologic potentiostat/galvanostat. All measurements were carried out at a constant temperature of 20 °C. The capacity values reported in this work include the contribution from carbon black, which corresponds to approximately 96 mA h g⁻¹ of the overall capacity of the electrodes.

Supplementary Information The online version contains supplementary material available at <https://doi.org/10.1007/s10008-021-04912-2>.

Acknowledgements The authors thank the Research Council of Norway for the funding of the work, under the contract no. 274969 (“Bio-degradable Li-ion battery anodes”) and Elkem for supplying the silica used in this study. Pei Na Kui, Agnes Digranes, Kristin Høydalsvik Wells and Magnus Følstad are acknowledged for their technical support. The Research Council of Norway is acknowledged for the support to the Norwegian Micro- and Nano-Fabrication Facility, NorFab, project number 245963/F50 and to the Norwegian Center for Transmission Electron Microscopy, NORTEM (197405/F50). We acknowledge DESY (Hamburg, Germany), a member of the Helmholtz Association HGF, for the provision of experimental facilities. Parts of this research were carried out at PETRA III and we would like to thank Dr. Alexander Schökel for assistance in using beamline P02.1 (proposal no. I-20181179 EC). The research leading to this result has been supported by the project CALIPSOplus under the Grant Agreement 730872 from the EU Framework Program for Research and Innovation HORIZON 2020.

Funding Open access funding provided by NTNU Norwegian University of Science and Technology (incl St. Olavs Hospital - Trondheim University Hospital). The authors would like to the Research Council of Norway, contract no. 274969 (“Bio-degradable Li-ion battery anodes”) and the EU Program for Research and Innovation HORIZON 2020, CALIPSO plus project (Grant Agreement 730872).

Declarations

Conflict of interest The authors have no competing interests.

Open Access This article is licensed under a Creative Commons Attribution 4.0 International License, which permits use, sharing, adaptation, distribution and reproduction in any medium or format, as long as you give appropriate credit to the original author(s) and the source, provide a link to the Creative Commons licence, and indicate if changes were made. The images or other third party material in this article are included in the article's Creative Commons licence, unless indicated otherwise in a credit line to the material. If material is not included in the article's Creative Commons licence and your intended use is not permitted by statutory regulation or exceeds the permitted use, you will need to obtain permission directly from the copyright holder. To view a copy of this licence, visit <http://creativecommons.org/licenses/by/4.0/>.

References

- European Commission (2018) Report on raw materials for battery applications. Commission Staff Working Document SWD.
- Huisman J, Ciuta T, Mathieux F, Bobba S, Georgitzikis K, Pennington D (2020) RMIS Raw materials in the battery value chain: final content for the raw materials information system: strategic value chains: batteries section. Publications Office of the European Union.
- Erk C, Brezesinski T, Sommer H, Schneider R, Janek J (2013) Toward silicon anodes for next-generation lithium ion batteries: a comparative performance study of various polymer binders and silicon nanopowders. *ACS Appl Mater Interfaces* 5(15):7299–7307
- Bourderau S, Brousse T, Schleich D (1999) Amorphous silicon as a possible anode material for Li-ion batteries. *J Power Sources* 81-82: 233–236
- Szczecz J, Jin S (2011) Nanostructured silicon for high capacity lithium battery anodes. *Energy Environ Sci* 4(1):56–72
- Ng S, Wang J, Wexler D, Konstantinov K, Guo Z, Liu H (2006) Highly reversible lithium storage in spheroidal carbon-coated silicon nanocomposites as anodes for lithium-ion batteries. *Angew Chem* 118(41):7050–7053
- Cui LF, Ruffo R, Chan CK, Peng H, Cui Y (2009) Crystalline-amorphous core-shell silicon nanowires for high capacity and high current battery electrodes. *Nano Lett* 9(1):491–495
- Ashuri M, He Q, Shaw LL (2015) Silicon as potential anode material for Li-ion batteries: where size, geometry and structure matter. *Nanoscale* 8:74–103
- Goldman JL, Long BR, Gewirth AA, Nuzzo RG (2011) Strain anisotropies and self-limiting capacities in single-crystalline 3D silicon microstructures: models for high energy density lithium-ion battery anodes. *Adv Funct Mater* 21(13):2412–2422
- Shi F, Song Z, Ross PN, Somorjai GA, Ritchie RO, Komvopoulos K (2016) Failure mechanisms of single-crystal silicon electrodes in lithium-ion batteries. *Nat Commun* 7(1):11886
- Casimir A, Zhang H, Ogoke O, Amine JC, Lu J, Wu G (2016) Silicon-based anodes for lithium-ion batteries: effectiveness of materials synthesis and electrode preparation. *Nano Energy* 27:359–376
- Xu ZL, Liu X, Luo Y, Zhou L, Kim JK (2017) Nanosilicon anodes for high performance rechargeable batteries. *Prog Mater Sci* 90:1–44
- Gao B, Sinha S, Fleming L, Zhou O (2001) Alloy formation in nanostructured silicon. *Adv Mater* 13(11):816–819
- Favors Z, Wang W, Bay H, George A, Ozkan M, Ozkan CS (2019) Stable cycling of SiO₂ nanotubes as high-performance anodes for lithium-ion batteries. *Sci Rep* 4:4605
- Subramaniam CM, Srinivasan NR (2019) Electrochemical characteristics of submicron-sized spherical mesoporous silica (SBA-15) as lithium battery anode. *Materialia* 5:100202
- Lener G, Otero M, Barraco DE, Leiva EPM (2018) Energetics of silica lithiation and its applications to lithium ion batteries. *Electrochim Acta* 259:1053–1058
- Gao C, Zhao H, Lv P, Wang C, Wang J, Zhang T, Xia Q (2014) Superior cycling performance of SiO_x/C composite with arrayed mesoporous architecture as anode material for lithium-ion batteries. *J Electrochem Soc* 161(14):A2216–A2221
- Lv P, Zhao H, Gao C, Zhang T, Liu X (2015) Highly efficient and scalable synthesis of SiO_x/C composite with core-shell nanostructure as high-performance anode material for lithium ion batteries. *Electrochim Acta* 152:345–351
- Zhang J, Zhang X, Zhang C, Liu Z, Zheng J, Zuo Y, Xue C, Li C, Cheng B (2017) Facile and efficient synthesis of a micro-sized SiO_x/C core-shell composite as anode material for lithium ion batteries. *Energy Fuel* 31(8):8758–8763
- Blanco MV, Renman V, Vullum-Bruer F, Svensson AM (2020) Nanostructured diatom earth SiO₂ negative electrodes with superior electrochemical performance for lithium ion batteries. *RSC Adv* 10(55):33490–33498
- Gu Z, Xia X, Liu C, Hu X, Chen Y, Wang Z, Liu H (2018) Yolk structure of porous C/SiO₂/C composite as anode for lithium-ion batteries with quickly activated SiO₂. *J Alloys Compd* 757:265–272
- Cui J, Cheng F, Lin J, Yang J, Jiang K, Wen Z, Sun J (2017) High surface area C/SiO₂ composites from rice husks as a high-performance anode for lithium ion batteries. *Powder Technol* 311:1–8
- Yao Y, Zhang J, Xue L, Huang T, Yu A (2011) Carbon-coated SiO₂ nanoparticles as anode material for lithium ion batteries. *J Power Sources* 196(23):10240–10243
- Li M, Yu Y, Li J, Chen B, Wu X, Tian Y, Chen P (2015) Nanosilica/carbon composite spheres as anodes in Li-ion batteries with excellent cycle stability. *J Mater Chem A* 3:1476–1482
- Yuan Z, Zhao N, Shi C, Liu E, He C, He F (2016) Synthesis of SiO₂/3D porous carbon composite as anode material with enhanced lithium storage performance. *Chem Phys Lett* 651:19–23
- Lener G, Garcia-Blanco AA, Furlong O, Nazzarro M, Sapag K, Barraco DE, Leiva EPM (2018) A silica/carbon composite as anode for lithium-ion batteries with a large rate capability: experiment and theoretical considerations. *Electrochim Acta* 279:289–300
- Nita C, Fullenwarth J, Monconduit L, Le Meins JM, Fioux P, Parmentier J, Matei Ghimbeu C (2019) Eco-friendly synthesis of SiO₂ nanoparticles confined in hard carbon: a promising material with unexpected mechanism for Li-ion batteries. *Carbon* 143:598–609
- Zhao Y, Wang LP, Sougrati MT, Feng Z, Leconte Y, Fisher A, Srinivasan M, Xu Z (2017) A review on design strategies for carbon based metal oxides and sulfides nanocomposites for high performance Li and Na ion battery anodes. *Adv Energy Mater* 7:1601424
- Li H, Zhou H (2012) Enhancing the performance of Li-ion batteries by carbon coating: present and future. *Chem Commun* 48(9):1201–1217
- Li R, Wang Y, Zhou C, Wang C, Ba X, Li X, Huang X, Liu J (2015) Carbon-stabilized high capacity ferrous oxide nanorod array for flexible solid-state alkaline battery-supercapacitor hybrid device with high environmental suitability. *Adv Funct Mater* 25(33):5384–5394
- Zhang WM, Wu XL, Hu JS, Guo YG, Wan LJ (2008) Carbon coated Fe₃O₄ nanospindles as superior anode material for lithium-ion batteries. *Adv Funct Mater* 18(24):3941–3946
- Liu H, Wang G, Wang J, Wexler D (2008) Magnetite/carbon core-shell nanorods as anode materials for lithium-ion batteries. *Electrochim Commun* 10(12):1879–1882
- Piao Y, Kim HS, Sung YE, Hyeon T (2010) Facile synthesis of magnetitenanocrystals embedded in carbon matrix as superior anode materials for lithium-ion batteries. *Chem Commun* 46(1):118–120
- Zhu GN, Liu HJ, Zhuang JH, Wang CX, Wang YG, Xia YY (2011) Carbon-coated nano-sized Li₄Ti₅O₁₂ nanoporous micro-sphere as anode material for high rate lithium-ion batteries. *Energy Environ Sci* 4(10):4016–4022
- Wang Y, Huang Z, Wang Y (2015) A new approach to synthesize MoO₂@C for high-rate lithium ion batteries. *J Mater Chem A* 3(42):21314–21320
- Read J, Foster D, Wolfenstine J, Behl W (2001) SnO₂-carbon composites for lithium-ion battery anodes. *J Power Sources* 96(2):277–281
- Bresser D, Paillard E, Kloepsch R, Krueger S, Fiedler M, Schmitz R, Baither D, Winter M, Passerini S (2013) Carbon coated ZnFe₂O₄ nanoparticles for advanced lithium-ion anodes. *Adv Energy Mater* 3(4):513–523
- Doeff MM, Wilcox JD, Kosteci R, Lau G (2006) Optimization of carbon coating on LiFePO₄. *J Power Sources* 163(1):180–184
- Persson K, Sethuraman VA, Hardwick LJ, Hinuma Y, Meng YS, van der Ven A, Srinivasan V, Kosteci R, Ceder G (2010) Lithium diffusion in graphitic carbon. *J Phys Chem Lett* 1(8):1176–1180
- Tachikawa H, Shimizu A (2006) Diffusion dynamics of the Li atom on amorphous carbon: a direct orbital-molecular dynamics study. *J Phys Chem B* 110(41):20445–20450

41. McDowell MT, Woo Lee S, Wang C, Cui Y (2012) The effect of metallic coatings and crystallinity on the volume expansion of silicon during electrochemical/lithiation/delithiation. *Nano Energy* 1(3):401–410
42. Cao X, Chuan X, Li S, Huang D, Cao G (2016) Hollow silica spheres embedded in a porous carbon matrix with superior performance as the anode for lithium-ion batteries. *Part Part Syst Charact* 33(2):110–117
43. Ban C, Kappes BB, Xu Q, Engtrakul C, Ciobanu CV, Dillon AC, Zhao Y (2012) Lithiation of silica through partial reduction. *Appl Phys Lett* 100(24):243905
44. Kim YK, Moon JW, Lee JG, Baek YK, Hong SH (2014) Porous carbon-coated silica macroparticles as anode materials for lithium ion batteries: effect of boric acid. *J Power Sources* 272:689–695
45. Lee S, Xu H (2019) Using powder XRD and pair distribution function to determine anisotropic atomic displacement parameters of orthorhombic tridymite and tetragonal cristobalite. *Acta Crystallogr B* 75(2):160–167
46. Lepoivre F, Larcher D, Tarascon JM (2016) Electrochemical activation of silica for enhanced performances of Si-based electrodes. *J Electrochem Soc* 163(13):A2791–A2796
47. Ogata K, Salager E, Kerr CJ, Fraser AE, Ducati C, Morris AJ, Hofmann S, Grey CP (2014) Revealing lithium-silicide phase transformations in nano-structured silicon-based lithium batteries via in situ NMR spectroscopy. *Nat Commun* 5:1–11
48. Agyeman DA, Song K, Lee GH, Park M, Kang YM (2016) Carbon-coated Si nanoparticles anchored between reduced graphene oxides as an extremely reversible anode material for high energy-density li-ion battery. *Adv Energy Mater* 6(20):1600904
49. Ferrari AC, Robertson J (2004) Raman spectroscopy of amorphous nanostructured, diamond-like carbon, and nanodiamond. *Philos Trans R Soc A Math Phys Eng Sci* 362(1824):2477–2512
50. Schwan J, Ulrich S, Batori V, Ehrhardt H, Silva SRP (1996) Raman spectroscopy on amorphous carbon films. *J Appl Phys* 80(1):440–447
51. Pardanaud C, Martin C, Giacometti G, Mellet N, Pégourié B, Roubin P (2015) Thermal stability and long term hydrogen/deuterium release from soft to hard amorphous carbon layers analyzed using in-situ Raman spectroscopy. Comparison with *torre supra* deposits. *Thin Solid Films* 581:92–98
52. Zhang X, Yan Q, Leng W, Li J, Zhang J, Cai Z, Hassan EB (2017) Carbon nanostructure of kraft lignin thermally treated at 500°C to 1000 °C. *Materials* 10(8):975
53. Jiu JT, Wang H, Cao CB, Zhu HS (1999) The effect of annealing temperature on the structure of diamond-like carbon films by electrodeposition technique. *J Mater Sci* 34(21):5205–5209
54. Kostecki R, Schnyder B, Alliata D, Song X, Kinoshita K, Kötzt R (2001) Surface studies of carbon films from pyrolyzed photoresist. *Thin Solid Films* 396(1-2):36–43
55. Wojdyr M (2010) Fityk: a general-purpose peak fitting program. *J Appl Crystallogr* 43(5):1126–1128

Publisher's note Springer Nature remains neutral with regard to jurisdictional claims in published maps and institutional affiliations.